Progress In Electromagnetics Research M, Vol. 134, 31–39, 2025 PIER M

(Received 29 March 2025, Accepted 17 June 2025, Scheduled 8 July 2025)

A Novel Strategy for Low Profile High-Impedance Ground Planes

Guoyan Wang[1], Hans Park[1, 2], and Sung Il Park[1, 3, *]

[1] *School of Biomedical Engineering, ShanghaiTech University, China*
[2] *College Station High School, TX, USA*
[3] *State Key Laboratory of Advanced Medical Materials and Devices, ShanghaiTech University, China*

ABSTRACT: A high-impedance ground plane has been proposed that enables the reflection of magnetic fields within a frequency range of interest. When being combined with loop coil antennas or H-field-oriented structures, it can boost transmission efficiency by up to 3 dB. Although several approaches, such as mushroom-shaped protuberant surfaces paired with capacitive loading, have been described to suppress surface waves at certain frequency ranges, the shift to a desired frequency range (e.g., from 5 GHz to 1 GHz) is marginal, and their form factors make these methods less ideal for applications in power and data communication. Here, we describe new strategies for a low-profile high-impedance ground plane. The insertion of a metal ground plane between the top and bottom mushroom-shaped surfaces reinforces capacitive couplings between adjacent unit cells. When being coupled with extended spiral paths, this configuration leads to an apparent change in the resonant frequency of the structure. Fabrication of the proposed structure demonstrates that the sandwiched metal ground plane, paired with extended spiral paths, leads to a noticeable shift in the resonant frequency toward lower sub-GHz ranges at given dimensions. Measurements are in good agreement with the results from the analytical model.

1. INTRODUCTION

The basic principle of a high-impedance surface (HIS) or ground plane is to suppress surface waves within a frequency range of interest using engineered structures such as mushroom-shaped unit cells [1]. The reflection phase of the HIS depends on both the value and type (inductive or capacitive) of the load impedance, and lumped loads can be used to design compact and tunable HIS [2]. Here, capacitive couplings and inductive current pathways between adjacent unit cells are key factors in the realization of high impedance at a certain frequency range [9]. These two factors also determine the resonant frequency of the structure, suggesting that the resonant frequency can be tuned by adjusting the gap between adjacent unit cells and/or height of the unit cell in the structure. However, this approach leads to an increase in their form factor. While capacitive loading techniques have been described to achieve a HIS at specific dimensions, the resulting shift in resonant frequency is marginal, making these approaches less ideal for practical applications [3].

To tackle this challenge, we introduced an inductive loading technique. Here, spiral loops inserted between the top and bottom layers extend the current pathways, thereby enhancing inductive coupling and consequently lowering the structure's resonant frequency [4]. Demonstrations revealed that a shift in the resonant frequency from a low GHz range to a sub-GHz range can be achieved without increasing the form factor.

In this study, we propose a new method to further lower the resonant frequency of the HIS. In this method, the metal ground plane is placed between the top and bottom mushroom-shaped layers. The proposed structure is equivalent to a stacked HIS structure, in which the middle metal ground plane is sandwiched between the two layers. In conventional HIS structures, both the top mushroom-shaped layer and bottom metal ground plane induce capacitive couplings between unit cells while routing surface currents through vias. This can be modeled as an equivalent circuit of a parallel resonant circuit, which offers an infinite or high surface impedance at the resonant frequency range.

However, in comparison to conventional HISs, capacitive couplings associated with the top mushroom-shaped layer are reinforced by the bottom mushroom-shaped layer in the proposed structure, rather than contributions by only the top layer in HISs. When being combined with extended spiral paths [7], this combinational approach results in a significant shift in the resonant frequency toward the sub-GHz range without an increase in form factor.

We demonstrated the proposed structure, and experimental measurements revealed that it significantly lowers the resonant frequency of the structure at given dimensions. The measurement results show strong agreement with those of numerical analysis and analytical modeling.

2. ANALYTICAL MODEL

A schematic illustration of the unit cell in the proposed structure is shown in Fig. 1. It consists of two windmill-shaped metallic patches on the top and bottom, a middle metal ground plane, and a square-shaped spiral path positioned between the

---

[*] Corresponding author: Sung Il Park (sipark@shanghaitech.edu.cn).

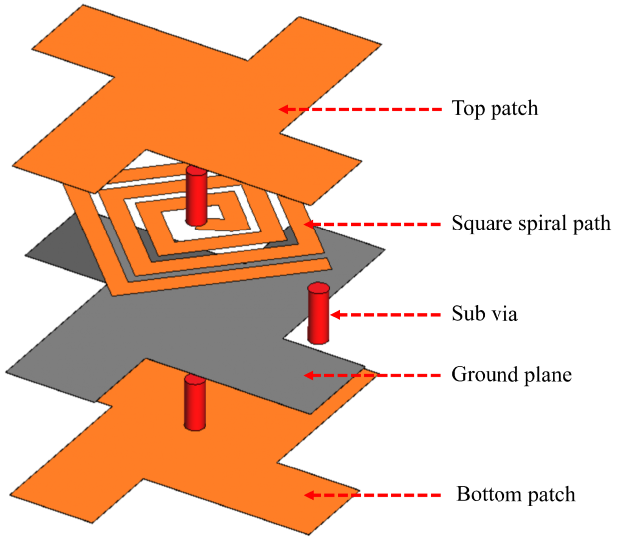

FIGURE 1. Schematic illustration of a unit cell in the proposed structure.

top patches and middle ground plane. The following elaborates on our analytical model.

2.1. Capacitance

Couplings between adjacent patches on the plane result in capacitance when $d \gg g$. As shown in Fig. 2, the fringe capacitance associated with adjacent patches can be calculated using conformal mapping [5]. The capacitances for windmill-shaped and square-shaped patches can be calculated using the following formulas, respectively. Here, C_1 is the capacitance of windmill-shaped patches, and C_2 is the capacitance of square-shaped patches.

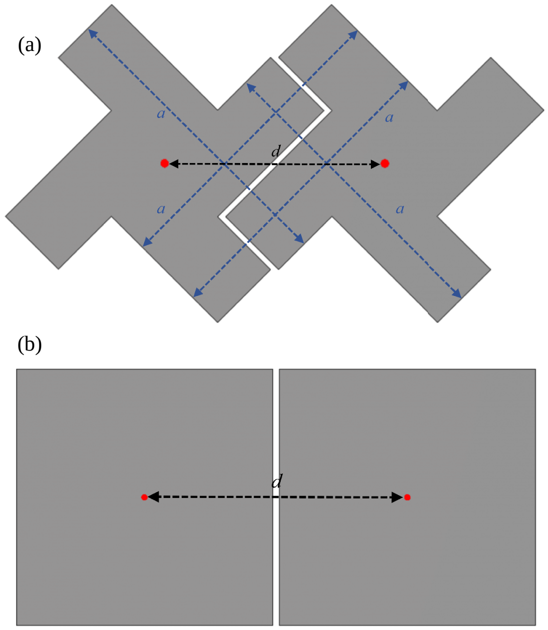

FIGURE 2. Top view of two-unit cells on the structure. (a) Proposed windmill-shaped patches. (b) Conventional square-shaped patches.

$$C_1 = \frac{(a-2g)\varepsilon_0(1+\varepsilon_r)}{\pi}\,\text{Cosh}^{-1}\left(\frac{a-g}{g}\right) \tag{1a}$$

$$a = \sqrt{2}d \tag{1b}$$

$$C_2 = \frac{(d-g)\varepsilon_0(1+\varepsilon_r)}{\pi}\,\text{Cosh}^{-1}\left(\frac{2d-g}{g}\right) \tag{1c}$$

where $\varepsilon_0 = 8.854 \times 10^{-12}$ [F/m] is the absolute permittivity, ε_r the relative dielectric constant of substrate, d the distance between the centers of adjacent unit cells, and g the gap.

Here, we calculate the increment in capacitance by comparing C_1 and C_2. Using Equations (1a)–(1c), we can derive the formula for the rate of increase in capacitance.

$$k = \frac{\left(\sqrt{2}d - 2g\right)\text{Cosh}^{-1}\left(\frac{\sqrt{2}d-g}{g}\right)}{(d-g)\text{Cosh}^{-1}\left(\frac{2d-g}{g}\right)} - 1. \tag{2}$$

Figure 3 compares the capacitance of windmill-shaped patches with that of square-shaped patches. It reveals that the capacitance of the windmill-shaped patches increases up to 35%. At a distance of 7.8 mm, an increase of 29.1% was achieved compared to the conventional square HIS.

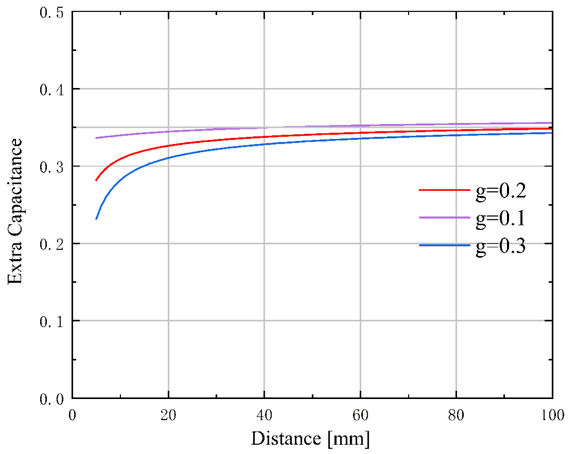

FIGURE 3. Enhancement of capacitance as a function of distance between two-unit cells at various g values (0.1 mm, 0.2 mm, and 0.3 mm).

2.2. Inductance

Figure 4 illustrates the current paths on the structure. The structure is modeled as two discrete inductors, L_1 and L_p. L_1 consists of top and bottom patches, middle ground plane, and sub-vias, while L_p is associated with the spiral coils.

The calculation of L_1 is straightforward [5].

$$L_1 = \mu_0 t \tag{3}$$

where $\mu_0 = 4\Pi \times 10^{-7}$ [H/m] is the absolute permeability, and t is the thickness of the substrate.

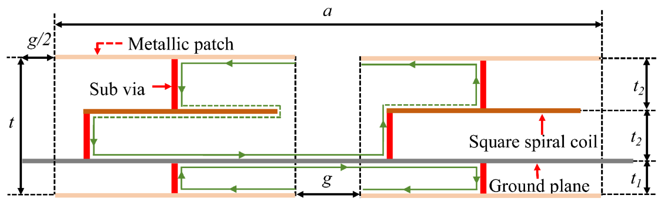

FIGURE 4. Illustration of current path formed by adjacent unit cells on the structure.

To calculate L_p, we use a monomial expression that is more accurate than the expression for square spiral inductance (Fig. 5) [6].

$$L_p = 1.62 \times 10^{-3} d_{\text{out}}^{-1.21} w^{-0.147} d_{\text{avg}}^{2.4} n^{1.78} s^{-0.03} \tag{4}$$

where d_{out}, d_{in}, w, and s represent the parameters of the square spiral inductor; n is the number of turns, and $d_{\text{avg}} = (d_{\text{out}} + d_{\text{in}})/2$.

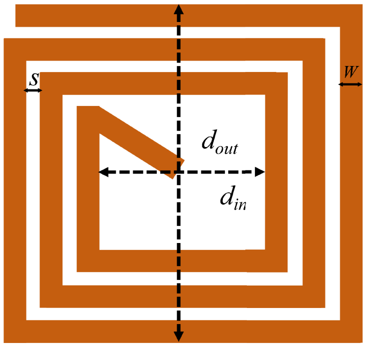

FIGURE 5. Top view of a square spiral loop with multi-turns.

Figure 4 shows the current direction on the structure. It indicates that the mutual inductance between adjacent spiral coils is $-L_p$, as the current path on one coil is opposite to that on the other [13, 19]. This leads to the total inductance of the proposed structures, which is expressed as follows.

$$L = L_1 + L_p \tag{5}$$

2.3. Resonant Frequency

Figure 6 illustrates the unit cell of the proposed three-layer structure and its equivalent circuit model. The impedance of a parallel resonant LC circuit is expressed in Equation (6) as follows.

$$Z = \frac{j\omega L}{1 - 2\omega^2 LC} \tag{6}$$

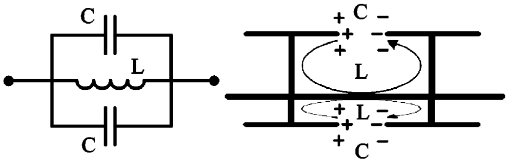

FIGURE 6. Equivalent LC circuit for a unit cell of the proposed three-layer HIS.

From Equation (6), we can calculate the resonant frequency using the basic circuit formula.

$$f_0 = \frac{1}{2\pi\sqrt{2LC}} \tag{7}$$

The impedance is high within a narrow range of resonant frequencies. In this frequency range, the structure suppresses both TM and TE surface waves. At frequencies lower than this range, the structure exhibits inductive behavior, suppressing TE waves and supporting TM waves. Conversely, at frequencies higher than this range, it exhibits capacitive behavior, suppressing TM waves and supporting TE waves. This relationship allows us to determine the bandwidth by analyzing the TM and TE waves.

3. SIMULATION RESULTS

We performed full-wave simulations using the commercial finite element analysis software, Computer Simulation Technology (CST), to verify the proposed design prior to fabrication. Two parallel coaxial probes were placed on either the top or bottom plane to measure the S_{12} parameters.

The transmission coefficient, S_{12}, as a function of the distance between the middle ground plane and bottom plane with respect to given frequency ranges is shown in Fig. 7. The results indicate that capacitive couplings between the ground and bottom plane are maximized at a certain distance.

Figures 8 & 9 illustrate the E-field and H-field distributions on the structure, respectively. Simulation results revealed that the bottom and middle ground planes, when being paired with the top two planes, enhance capacitive coupling (Fig. 8). In contrast, inductive couplings associated with the two bottom planes are negligible (Fig. 9).

Next, we conducted simulations on the structures with a probe placed on the bottom plane. The series of numerical analyses can facilitate understanding of responses at the other half of the proposed structure (Fig. 10). As expected, the resonant frequency shifted toward a value higher than 4 GHz. This finding indicates that inductive couplings associated with spiral paths are negligible and do not contribute to the reduction of the resonant frequency.

4. EXPERIMENTAL RESULTS

As shown in Fig. 11, we fabricated four structures using a standard printed circuit board manufacturer. Each sample has 18×18 cells, and their unit-cell dimensions are given in Fig. 1. The proposed HIS structure comprises a ground plane near the bottom patch on an FR-4 substrate (0.3 mm thickness) and an FR-4 substrate (4 mm thickness) with a spiral path in the middle of the top layer. The radius of the micro-vias drilled in the substrate is 297 µm. The distance between the centers of adjacent patches is 7.8 mm. The gap between the adjacent unit cells is 0.2 mm. The parameters of the fabricated HIS are the same as those used for simulations. Other HIS samples differ in the thickness of the bottom & top layers. The total thickness of both substrates is 4.3 mm.

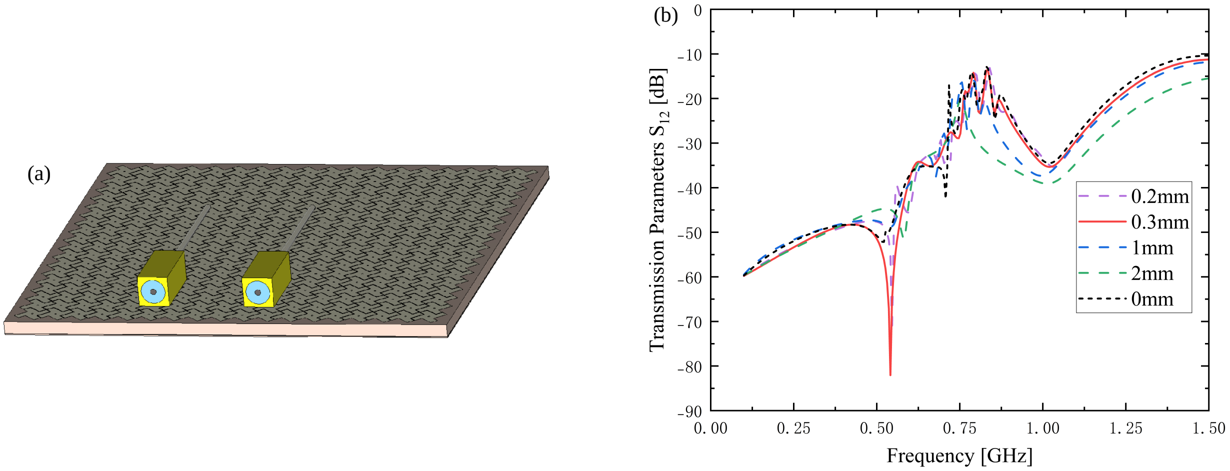

FIGURE 7. (a) Illustration of location of probes relative to the structure. (b) Plots of S_{12} as a function of the distance between the middle ground plane and the bottom plane with respect to given frequency ranges.

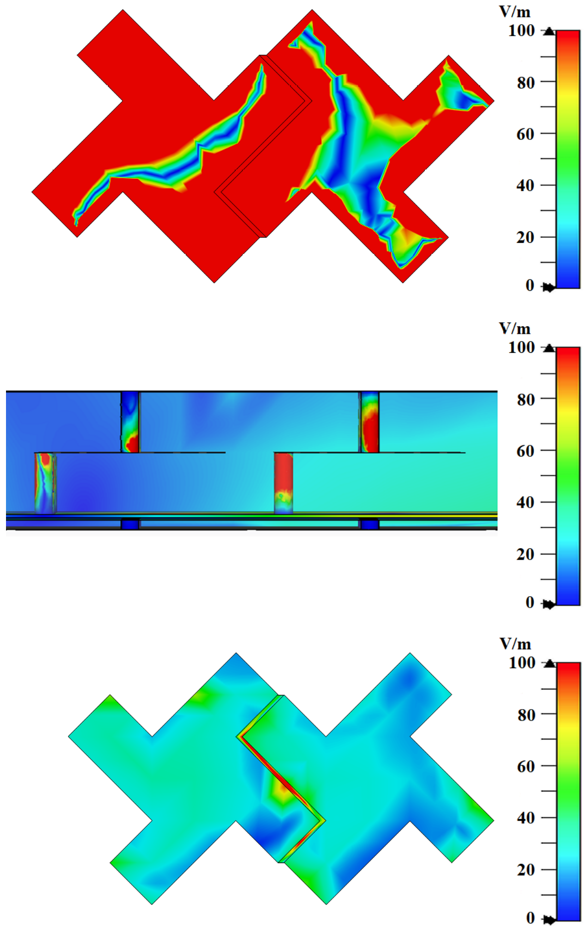

FIGURE 8. E-field distributions on the top layer, vias and bottom layer of the proposed structure, where the distance between the middle and the bottom layer is 0.3 mm.

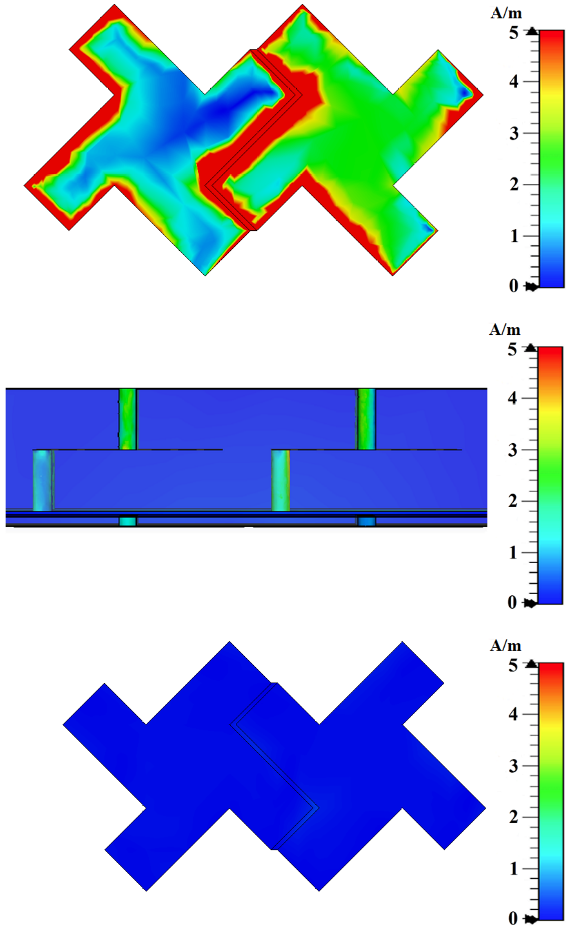

FIGURE 9. H-field distributions on the top layer, vias, and bottom layer of the proposed structure, where the distance between the middle and the bottom layer is 0.3 mm.

The experimental setup for surface wave measurements is illustrated in Fig. 12. Here, a vector network analyzer (VNA, SIGLENT SHA861A) is connected to a pair of coaxial probe antennas, which are positioned either vertically or parallel to the high-impedance surface to capture TM/TE surface-wave propagation and measure the S_{12} transmission coefficient. The VNA is calibrated using the standard SOLT method to account for connector and cable losses, ensuring accurate measurements.

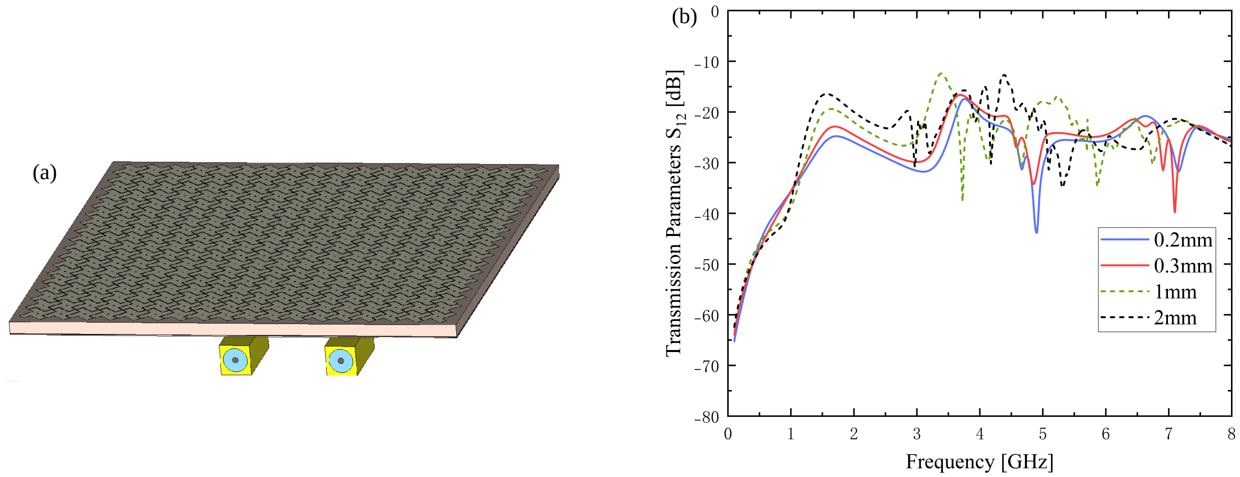

FIGURE 10. (a) Illustration of location of probes relative to the structure. (b) Plots of S_{12} as a function of distance between the middle ground plane and the bottom plane. Here, probes are located on the bottom plane.

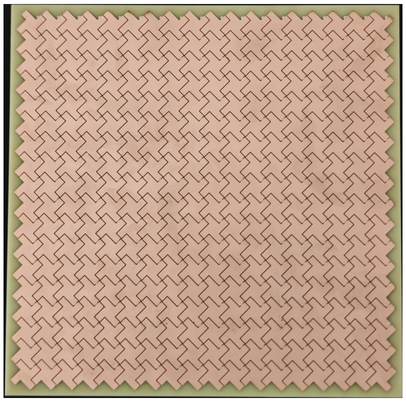

FIGURE 11. Top view of the fabricated windmill shaped three-layer HIS.

Impedance matching for the probe antennas was achieved by following established techniques for measuring TM and TE waves, which are widely used in the measurement of HIS [1, 2]. To minimize mismatches and reflections, the position and orientation of the probes are carefully adjusted. Both experiments and simulations confirmed that a range of frequency for measurements is ensured at a distance of approximately 5 mm from the substrate. Figs. 13 & 14 show the measured TM & TE surface wave transmission coefficients of each sample.

As shown in Figs. 13 & 14, the resonant frequency shifts toward a lower frequency range (from 0.9 GHz to 0.59 GHz) as the middle ground plane is moved closer to the bottom patches. This suggests that the shift in the resonant frequency is due to contributions by the 1) enhanced inductance associated with the extension of current paths between top and middle layers and 2) enhanced capacitive couplings between the middle and bottom layers.

Resonant frequency comparisons of TM & TE surfaces for both structures are highlighted in Fig. 15. At given dimensions, the resonant frequency of the proposed HIS is decreased by 30% in comparison to the conventional HIS.

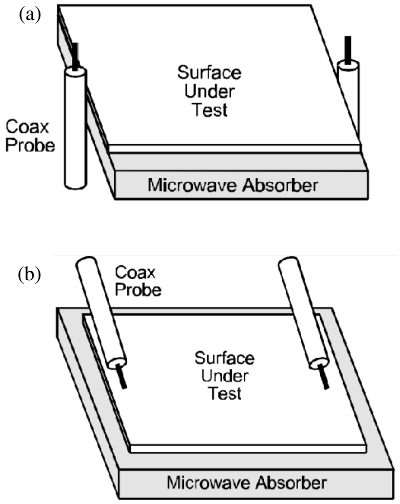

FIGURE 12. (a) TM surface-wave measurement. (b) TE surface-wave measurement.

TABLE 1. Summary of the geometrical parameters.

d	g	ε_r	w	s	n	d_{out}	d_{in}
7.8	0.2	4.6	0.594	0.256	3	6.188	1.6

Tables 1 & 2 summarize the results of the geometrical parameters and resonance frequencies obtained from analytical and numerical methods, as well as measurements. As expected, the proposed analytical model is in agreement with the numerical method and experimental results, though there may exist some discrepancies between the model and experimental results. Here, the discrepancies between the measurements and analytical model are mainly due to the parasitic capacitance of the adjacent elements, including spiral coils, metal patches, and ground planes.

Table 3 shows the comparisons of the proposed structure to conventional HISs (windmill-shaped and square-shaped unit cells). In comparison to the conventional two-layer structure,

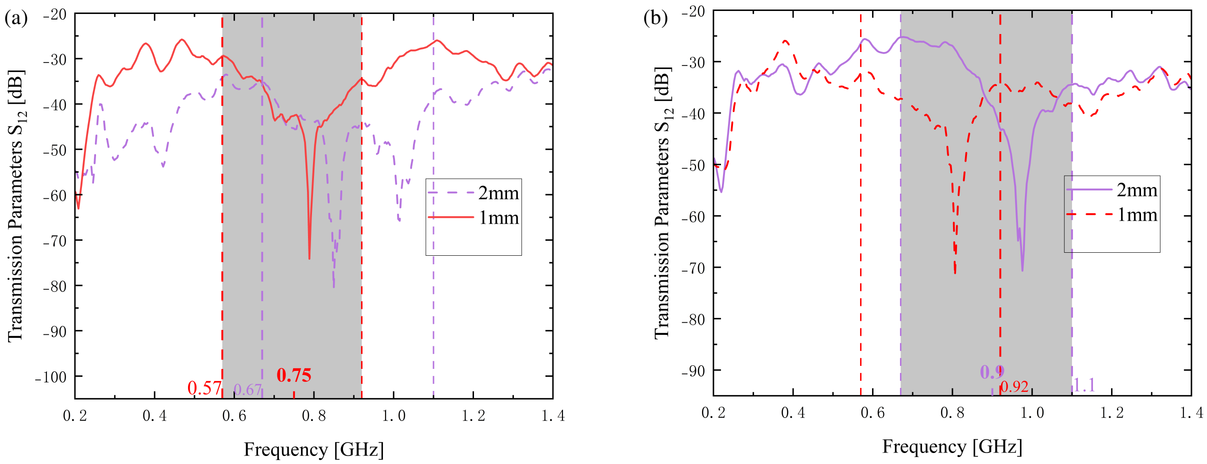

FIGURE 13. Plots of (a) TM and (b) TE surface wave transmission coefficients as a function of the distance between the middle ground plane and the bottom plane with respect to given frequency ranges.

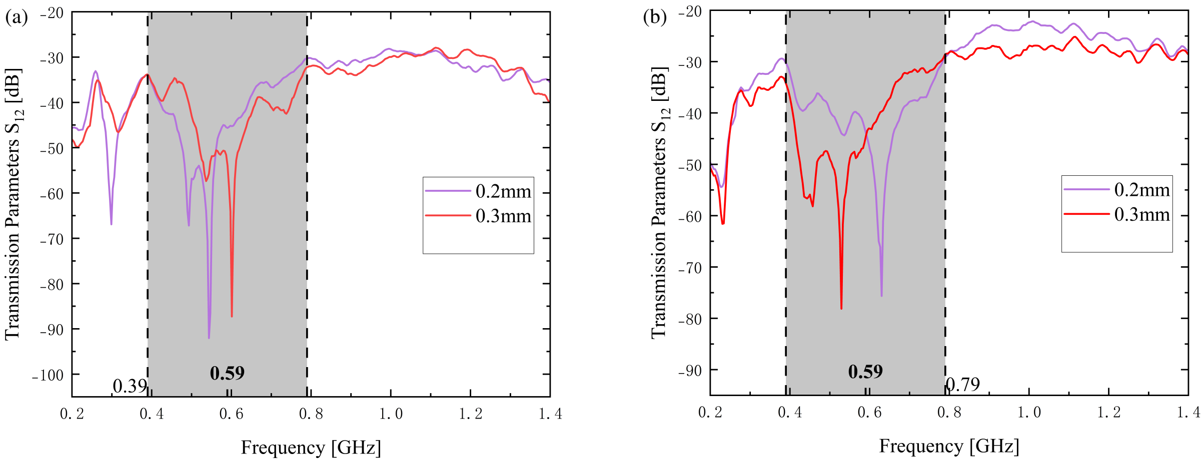

FIGURE 14. Plots of (a) TM and (b) TE surface wave transmission coefficients as a function of the distance between the middle ground plane and the bottom plane with respect to given frequency ranges.

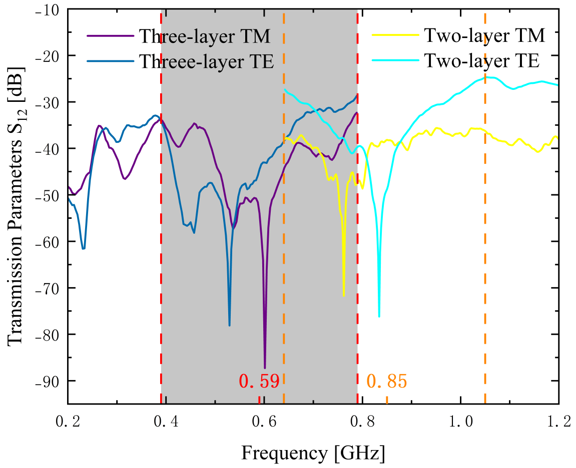

FIGURE 15. Plots of TM and TE surface wave transmission coefficients of the proposed two-layer & three-layer HIS.

the three-layer HIS reduces the resonant frequency by 30%. Additionally, the resonant frequency of the three-layer HIS decreases by 37%.

The dielectric constant and loss tangent of the FR-4 substrate are 4.6 and 0.018, respectively. We used these parameters for simulations in CST to ensure consistency with the fabricated HIS. Variations in the dielectric constant and loss tangent in our simulations are illustrated in Fig. 16. Simulation results show that the differences in the dielectric constant and loss tangent are less than 0.2 (4.35%) and 10%, respectively.

Capacitive couplings between adjacent patches are reinforced as the dielectric constant of the substrate increases. To highlight the effect of dielectric constant on the shift of resonant frequency, we define the following formula.

$$\frac{\Delta f}{f} \propto \frac{\sqrt{1+\varepsilon_r+\Delta\varepsilon}-\sqrt{1+\varepsilon_r}}{\sqrt{1+\varepsilon_r+\Delta\varepsilon}} \tag{8}$$

where ε_r is the standard dielectric constant, f the standard resonant frequency, $\Delta\varepsilon$ the difference between the standard dielectric constant and frequency-dependent dielectric constan, and Δf the difference in resonant frequency between the standard and frequency-dependent dielectric constant.

TABLE 2. Summary of the resonant frequencies.

	Method	$t_1 = 0.2$	$t_1 = 0.3$	$t_1 = 1$	$t_1 = 2$
Resonant Frequency	Analytical	0.62	0.62	0.89	0.9
	Numerical	0.54	0.54	0.96	0.99
	Measurement	0.59	0.59	0.75	0.9

TABLE 3. Comparisons of the proposed structure with conventional HISs.

	Structure	Three-layer	Two-layer	Conventional square
Modeling Estimation	Capacitance [pF]	1.56	0.78	0.60
	Inductance [nH]	42.04	42.41	42.41
Resonant Frequency [GHz]	Analytical	0.62	0.88	0.99
	Measurement	0.59	0.85	\

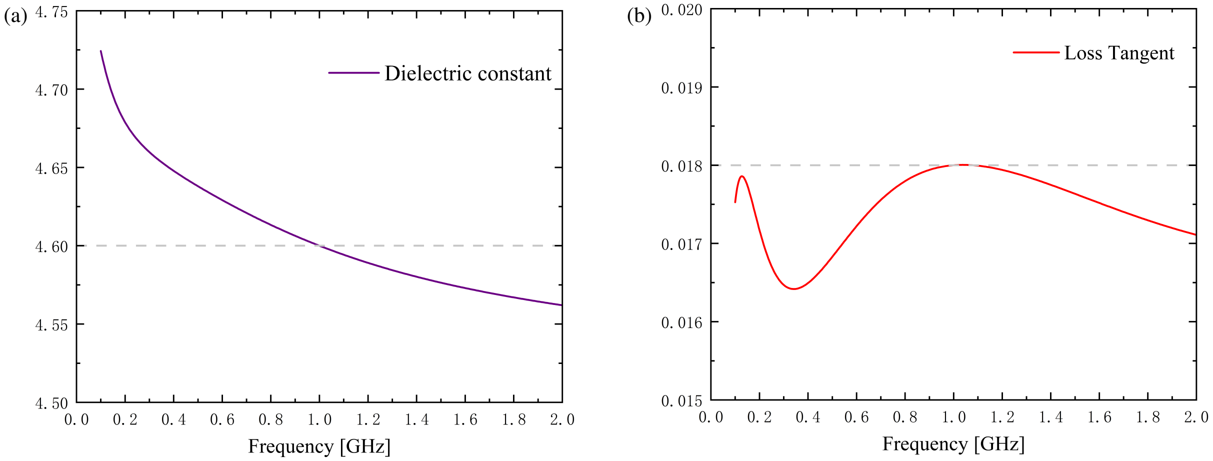

FIGURE 16. Variations in (a) dielectric constant and (b) loss tangent.

We found that the variation in frequency is less than 0.88%, suggesting that the influence of deviations in the dielectric constant can be negligible.

5. DISCUSSION

The strategies described in this study can enable the realization of sub-GHz range HIS at dimensions comparable to those of smartphone devices. A straightforward extension of this technology is to achieve HIS in the high-frequency (MHz) range. Resonant or inductive coupling-based wireless power transmission systems operating in the high-frequency range have been demonstrated for biomedical applications [10]. In such systems, electromagnetic waves at tens of MHz are transmitted through coil-shaped antennas in the air. A receiver implanted in an animal harvests radio frequency power from the coil antenna to operate an electronic system embedded within the receiver. In these applications, wireless coverage is crucial for the success of the experiment.

To enhance wireless coverage, one might simply increase the transmission power. However, the increase in received power associated with higher transmitted power would be marginal due to the nature of electromagnetic waves at high frequencies (MHz) [13]. This limitation can be problematic. For example, an open area for monitoring locomotor activities typically has dimensions of $60 \times 60\,\text{cm}^2$, and the transmission coil antenna should provide sufficient wireless coverage for the entire area [11, 12]. However, in the experimental setup, the range of received powers spans about two orders of magnitude, indicating that the device on an animal may not receive enough power for operation when being positioned in the middle of the coil antenna [14]. When the device is combined with HIS, the received power can be enhanced by up to 3 dB. If we employ the proposed design, HIS can be realized within a $60 \times 60\,\text{cm}^2$ area. The structure has a low profile and can be placed at the bottom of the arena or experimental apparatus. This placement also helps to minimize interference associated with increased TX power.

In general, as the array incorporates more unit cells, it provides a more uniform field distribution. Enhanced capacitive couplings from the top and bottom layers lead to a shift in a resonant frequency toward the lower frequency range. This suggests that the proposed design can accommodate more unit cells than conventional HIS designs, and thereby offers better performance at given dimensions than conventional HIS designs.

While the contributions of current paths defined by the bottom layer and metal ground layer to an increase in inductance are negligible, the capacitive couplings linked to these two layers are significant. This is because the top HIS suppresses or reflects magnetic waves. To test this hypothesis, we ran simulations using CST, a commercially available FEM analysis tool. Numerical analysis results revealed that the insertion of spiral loops between the metal and bottom layers does not contribute to the shift in the resonant frequency compared to an HIS without spiral loops. The E and H field distributions on the bottom two layers support this finding. This indicates that the reinforced capacitive couplings associated with the top and bottom layers outweigh (or at least compensate) the loss linked to the shortened inductive paths defined by the top and bottom metal planes.

This sets guidelines for the design of HIS. For example, a structure where the metal ground plane is closer to the bottom layer can accommodate longer current pathways than a structure where the metal ground layer is closer to the top layer. This will minimize the loss associated with longer current pathways in the upper layer (inductive loadings) while enhancing capacitive couplings in the bottom layer. Similarly, one can employ an interdigitated surface structure in the bottom layer to enhance capacitive couplings or other techniques [15–18]. Although fractal geometries are effective in enhancing the surface inductance of structures, an analytical model to guide their design at sub-GHz frequencies is not available. In contrast, the proposed approach offers an analytical model that enables accurate and efficient designs of high-impedance surfaces (HISs) with broader and more practical bandwidths [8]. By integrating a metal ground plane and spiral loops in the upper layer, the proposed HIS could achieve a HIS operating at MHz ranges at given dimensions, in a way that is impossible with existing methods. With a quantitative approach, the proposed design allows precise customization for the desired frequency range. While fractal HIS designs, characterized by a narrow bandwidth and a higher Q-factor ($Q = f_0/\Delta f$, where f_0 is the resonant frequency and Δf is the bandwidth), are well suited for narrowband surface wave suppression, the proposed HIS excels in suppressing surface waves across a broader frequency range, offering greater versatility and wider applicability.

Most studies on HIS structures focus on traditional designs, which lack insight into how electromagnetic wave propagation, material parameters, and structural features influence performance. A novel perspective is introduced by connecting wave equations with number theory, which provides insight into electromagnetic wave propagation [20, 21]. Material selection strategies are inspired by the suggestion of using graded porous materials, such as those derived from biomass, to optimize HIS performance [25]. Additionally, soliton theory and bifurcation analysis are valuable tools for understanding wave localization and parameter stability in HIS [22–24]. A deeper understanding of HIS functionality could facilitate HIS design with greater accuracy and quantitative precision.

6. CONCLUSION

We proposed a new method for decreasing the resonant frequency of conventional mushroom-shaped high-impedance surfaces (HIS) without increasing their dimensions. The reduction in the resonant frequency is due to the capacitive coupling between the bottom metal patches. We demonstrated that this capacitive coupling from the bottom plane is maximized at a certain distance between the middle and bottom planes. Experimental measurements are consistent with the numerical analysis and analytical model, respectively. The proposed structure offers potential for a wide range of applications in wireless communication and wireless power transfer.

REFERENCES

[1] Sievenpiper, D., L. Zhang, R. F. J. Broas, N. G. Alexopolous, and E. Yablonovitch, "High-impedance electromagnetic surfaces with a forbidden frequency band," *IEEE Transactions on Microwave Theory and Techniques*, Vol. 47, No. 11, 2059–2074, 1999.

[2] Broas, R. F. J., D. F. Sievenpiper, and E. Yablonovitch, "A high-impedance ground plane applied to a cellphone handset geometry," *IEEE Transactions on Microwave Theory and Techniques*, Vol. 49, No. 7, 1262–1265, 2001.

[3] Durgun, A. C., C. A. Balanis, C. R. Birtcher, H. Huang, and H. Yu, "High-impedance surfaces with periodically perforated ground planes," *IEEE Transactions on Antennas and Propagation*, Vol. 62, No. 9, 4510–4517, 2014.

[4] Gu, M., D. Vorobiev, W. S. Kim, H.-T. Chien, H.-M. Woo, S. Hong, and S. I. Park, "A novel approach using an inductive loading to lower the resonant frequency of a mushroom-shaped high impedance surface," *Progress In Electromagnetics Research M*, Vol. 90, 19–26, 2020.

[5] Sievenpiper, D., "High-impedance electromagnetic surfaces," Ph.D. dissertation, Dept. Elect. Eng., Univ. California at Los Angeles, Los Angeles, CA, USA, 1999.

[6] Mohan, S. S., M. d. M. Hershenson, S. P. Boyd, and T. H. Lee, "Simple accurate expressions for planar spiral inductances," *IEEE Journal of Solid-State Circuits*, Vol. 34, No. 10, 1419–1424, 1999.

[7] Hong, S., W. S. Kim, and S. I. Park, "Design of an inductive spiral-loop loaded unit cell in a mushroom-shaped high impedance surface for sub-GHz applications," *Progress In Electromagnetics Research M*, Vol. 100, 1–11, 2020.

[8] Gupta, A. K., H. C. Mohanta, P. S. R. Chowdary, M. V. Krishna, and H. G. Mohamed, "Design and analysis of fractal-shaped high-impedance surface unit cell characteristics," *Fractal and Fractional*, Vol. 7, No. 6, 472, 2023.

[9] Clavijo, S., R. E. Diaz, and W. E. McKinzie, "Design methodology for Sievenpiper high-impedance surfaces: An artificial magnetic conductor for positive gain electrically small antennas," *IEEE Transactions on Antennas and Propagation*, Vol. 51, No. 10, 2678–2690, 2003.

[10] Park, S. I., "Enhancement of wireless power transmission into biological tissues using a high surface impedance ground plane," *Progress In Electromagnetics Research*, Vol. 135, 123–136, 2012.

[11] Woo, H.-M., W. S. Kim, S. Hong, V. Jeevakumar, C. M. Smithhart, T. J. Price, B.-J. Yoon, and S. I. Park, "Machine learning enabled adaptive wireless power transmission system for neuroscience study," in *2020 54th Asilomar Conference on Signals, Systems, and Computers*, 808–812, Pacific Grove, CA, USA,

2020.

[12] Kim, W. S., S. Hong, M. Gamero, V. Jeevakumar, C. M. Smithhart, T. J. Price, R. D. Palmiter, C. Campos, and S. I. Park, "Organ-specific, multimodal, wireless optoelectronics for high-throughput phenotyping of peripheral neural pathways," *Nature Communications*, Vol. 12, No. 1, 157, 2021.

[13] Mickle, A. D., S. M. Won, K. N. Noh, J. Yoon, K. W. Meacham, Y. Xue, L. A. McIlvried, B. A. Copits, V. K. Samineni, K. E. Crawford, *et al.*, "A wireless closed-loop system for optogenetic peripheral neuromodulation," *Nature*, Vol. 565, No. 7739, 361–365, 2019.

[14] Kim, W. S., M. I. Khot, H.-M. Woo, S. Hong, D.-H. Baek, T. Maisey, B. Daniels, P. L. Coletta, B.-J. Yoon, D. G. Jayne, *et al.*, "AI-enabled, implantable, multichannel wireless telemetry for photodynamic therapy," *Nature Communications*, Vol. 13, No. 1, 2178, 2022.

[15] Kaipa, C. S. R., A. B. Yakovlev, S. I. Maslovski, and M. G. Silveirinha, "Mushroom-type high-impedance surface with loaded vias: Homogenization model and ultra-thin design," *IEEE Antennas and Wireless Propagation Letters*, Vol. 10, 1503–1506, 2011.

[16] Costa, F., S. Genovesi, and A. Monorchio, "On the bandwidth of high-impedance frequency selective surfaces," *IEEE Antennas and Wireless Propagation Letters*, Vol. 8, 1341–1344, 2009.

[17] Vallecchi, A., J. R. D. Luis, F. Capolino, and F. D. Flaviis, "Low profile fully planar folded dipole antenna on a high impedance surface," *IEEE Transactions on Antennas and Propagation*, Vol. 60, No. 1, 51–62, 2012.

[18] Shoute, G. and D. W. Barlage, "Fractal loop inductors," *IEEE Transactions on Magnetics*, Vol. 51, No. 6, 1–8, 2015.

[19] Hussain, I. and D.-K. Woo, "Simplified mutual inductance calculation of planar spiral coil for wireless power applications," *Sensors*, Vol. 22, No. 4, 1537, 2022.

[20] Yang, X.-J., A. A. Alsolami, and A. R. Ali, "An even entire function of order one is a special solution for a classical wave equation in one-dimensional space," *Thermal Science*, Vol. 27, No. 1B, 491–495, 2023.

[21] Ali, A. R., H. O. Roshid, S. Islam, and A. Khatun, "Analyzing bifurcation, stability, and wave solutions in nonlinear telecommunications models using transmission lines, Hamiltonian and Jacobian techniques," *Scientific Reports*, Vol. 14, No. 1, 15282, 2024.

[22] Ali, A. R., M. N. Alam, and M. W. Parven, "Unveiling optical soliton solutions and bifurcation analysis in the space-time fractional Fokas-Lenells equation via SSE approach," *Scientific Reports*, Vol. 14, No. 1, 2000, 2024.

[23] Islam, S., B. Halder, and A. R. Ali, "Optical and rogue type soliton solutions of the (2+1) dimensional nonlinear Heisenberg ferromagnetic spin chains equation," *Scientific Reports*, Vol. 13, No. 1, 9906, 2023.

[24] Khan, M. H., S. Islam, and A. R. Ali, "Certain results associated with lump and periodic-soliton solutions for (2+1)-D Calogero-Bogoyavlenskii-Schiff equation," *Journal of Applied Mathematics and Statistical Analysis*, Vol. 4, No. 2, 43–57, 2023.

[25] Khan, M., F. Mahmood, M. Ali, Y. Wang, A. R. Ali, and A. H. Majeed, "Synthesis of hierarchical porous carbon scaffold derived from red kidney bean peels for advanced Li-Se and Na-Se batteries," *Scientific Reports*, Vol. 14, No. 1, 17749, 2024.